Intensification of Precipitation Extremes with Warming in a Cloud-Resolving Model

CAROLINE J. MULLER AND PAUL A. O'GORMAN

Massachusetts Institute of Technology, Cambridge, Massachusetts

LARISSA E. BACK

University of Wisconsin—Madison, Madison, Wisconsin

ABSTRACT

A cloud-resolving model is used to investigate the effect of warming on high percentiles of precipitation (precipitation extremes) in the idealized setting of radiative-convective equilibrium. While this idealized setting does not allow for several factors that influence precipitation in the tropics, it does allow for an evaluation of the response of precipitation extremes to warming in simulations with resolved rather than parameterized convection. The methodology developed should also be applicable to less idealized simulations.

Modeled precipitation extremes are found to increase in magnitude in response to an increase in sea surface temperature. A dry static energy budget is used to relate the changes in precipitation extremes to changes in atmospheric temperature, vertical velocity, and precipitation efficiency. To first order, the changes in precipitation extremes are captured by changes in the mean temperature structure of the atmosphere. Changes in vertical velocities play a secondary role and tend to weaken the strength of precipitation extremes, despite an intensification of updraft velocities in the upper troposphere. The influence of changes in condensate transports on precipitation extremes is quantified in terms of a precipitation efficiency; it does not change greatly with warming.

Tropical precipitation extremes have previously been found to increase at a greater fractional rate than the amount of atmospheric water vapor in observations of present-day variability and in some climate model simulations with parameterized convection. But the fractional increases in precipitation extremes in the cloud-resolving simulations are comparable in magnitude to those in surface water vapor concentrations (owing to a partial cancellation between dynamical and thermodynamical changes), and are substantially less than the fractional increases in column water vapor.

1. Introduction

Increases in the frequency of heavy precipitation events are potentially one of the most important impacts on society of the changing hydrological cycle under global warming. Global mean precipitation is thought to be constrained energetically and increases at a modest rate of about 2% K^{-1} (Allen and Ingram 2002; Held and Soden 2006; O'Gorman and Schneider 2008), but extreme precipitation events are not limited by the global energy budget and could increase at a greater rate under warming. It has previously been argued that precipitation extremes should increase with warming because of the greater amount of water vapor in a warmer atmosphere (Trenberth 1999; Allen and Ingram 2002; Pall et al. 2007). Indeed, tropical precipitation rates and column water vapor are known to be tightly coupled in the present climate (e.g., Bretherton et al. 2004; Neelin et al. 2009; Muller et al. 2009). Climate models predict only marginal changes in relative humidity with global warming, implying that water vapor concentrations increase following the Clausius–Clapeyron relation. The resulting rates of change in zonal mean column water vapor range from 6% to 12% K^{-1} depending on latitude, with somewhat lower fractional rates of change for surface water vapor concentrations (O'Gorman and Muller 2010).

The thermodynamic dependence of precipitation rates can be estimated by considering the condensation rate for an adiabatically lifted air parcel (Iribarne and Godson 1981, see section 9.14; O'Gorman and Schneider 2009a,b). This results in an approximate expression for precipitation

Corresponding author address: Caroline J. Muller, Earth, Atmospheric, and Planetary Sciences, Massachusetts Institute of Technology, 77 Massachusetts Ave., Cambridge, MA 02139-4307.
E-mail: mullerc@mit.edu

rates that depends on the vertical gradient of saturation specific humidity along a moist adiabat, and suggests that tropical precipitation extremes can be expected to scale more closely with surface rather than column water vapor. A scaling for precipitation extremes (defined as high percentiles of the precipitation distribution), which includes this thermodynamic dependence and a dynamical contribution, has been used to evaluate changes in precipitation extremes in a wide range of climate model simulations (O'Gorman and Schneider 2009a,b; Sugiyama et al. 2010). The dynamical contribution arises because precipitation extremes are proportional to the associated pressure vertical velocity (e.g., Iribarne and Godson 1981). Increases in vertical velocity likely explain the results of some observational studies, which find rates of increase of precipitation extremes with warming that are greater than expected from thermodynamic considerations alone (Allan and Soden 2008; Lenderink and van Meijgaard 2008; Liu et al. 2009). Results from climate change simulations in general circulation models (GCMs) consistently point to little change in the vertical velocities associated with precipitation extremes in the extratropics, but give widely divergent changes in vertical velocities in the tropics (Emori and Brown 2005; O'Gorman and Schneider 2009a; Sugiyama et al. 2010). For example, O'Gorman and Schneider (2009a) found that the rate of increase of tropical precipitation extremes in the third Coupled Model Intercomparison Project (CMIP3) climate model simulations ranged from 1.3% to 30% K^{-1} depending on the climate model, and that this intermodel scatter was primarily due to different changes in vertical velocities.

The inability of current climate models to consistently predict changes in tropical precipitation extremes with warming is likely tied to the use of convective parameterizations (Wilcox and Donner 2007), and is not surprising given the failure of the climate models to simulate observed tropical precipitation extremes in the present climate (Kharin et al. 2007). It is sometimes argued that increased latent heating in a warmer climate must fuel stronger updraft velocities, but this does not have to be the case since the mean static stability of the atmosphere also changes with warming (Del Genio et al. 2007). Arguments for decreases in the magnitude of the vertical overturning circulation in the tropics have also been proposed (Betts 1998; Held and Soden 2006; Vecchi and Soden 2007).

Since simulations of tropical precipitation extremes with current global climate models are unreliable, progress on the problem of changing tropical precipitation extremes must rely on either theory, observations, or simulations that resolve the convective-scale processes. In this paper, we describe the changes in precipitation extremes that occur with warming in simulations with a cloud-resolving model (CRM; sometimes referred to as a cloud system–resolving model). We compare the precipitation extremes in a control simulation and in a simulation with a higher sea surface temperature (SST) to address the following questions:

- How much do precipitation extremes increase with warming?
- Are there substantial changes in the magnitudes of the vertical velocities associated with these precipitation extremes?
- Can we derive a simple expression that makes explicit the thermodynamic and dynamic contributions to precipitation extremes, and that takes into account the resolved convective dynamics and condensate transports?

We run the CRM in an idealized setting over fixed SST, with periodic boundary conditions in the horizontal, prescribed radiative cooling, no large-scale forcing or rotation and a relatively large domain (1024 km × 1024 km). Other factors may affect precipitation extremes, such as large-scale dynamics, land–ocean contrasts (e.g., Williams et al. 2004), orography (e.g., Roe 2005), radiation–convection interactions (e.g., Fu et al. 1995), rotational effects, and convective organization (tropical cyclones being an important example), but these are beyond the scope of this study. Our methodology could also be applied to more realistic regional cloud-resolving model simulations, but it seems likely that results would depend on uncertain boundary conditions and be more complicated to evaluate and interpret. We chose to look at an idealized analog to climate change for ease of interpretation, to build intuition and to allow our results to be potentially generalizable.

After introducing the CRM and simulations (section 2), we describe the changes in precipitation extremes in response to increased surface temperature (section 3). An expression relating changes in precipitation extremes to dynamic and thermodynamic variables is derived from the dry static energy budget (section 4) and used to diagnose the different contributions to the changes in precipitation extremes; it is similar to the scaling in O'Gorman and Schneider (2009b) but includes a precipitation efficiency factor and the convective-scale vertical velocity. We investigate the sensitivity of our results to the radiative cooling profile in order to probe the relationship between changes in mean and extreme precipitation (section 5). We then analyze the changes in vertical velocities associated with precipitation extremes (section 6), followed by our conclusions (section 7).

2. Model and simulations

The model used is a version of the System for Atmospheric Modeling [SAM; see Khairoutdinov and Randall

(2003) for a detailed description]. The prognostic thermodynamic variables of the model are liquid water/ice moist static energy, total nonprecipitating water (vapor + cloud liquid water + cloud ice), and total precipitating water (rain + snow + graupel). The liquid water/ice moist static energy is conserved during moist adiabatic processes in the model, including the freezing and melting of precipitation.

The choice of the horizontal domain size and spatial resolution is made difficult by the need to adequately resolve the convection and yet not limit it by having too small a domain. Paulus and Garner (2006) found that intense upward vertical velocities in simulations of radiative–convective equilibrium were not yet fully converged for horizontal resolutions as small as 2 km, while Parodi and Emanuel (2009) found that these velocities were not yet fully converged as the domain size was increased up to 400 km. In an attempt to allow for possible convective organization (cf. Bretherton et al. 2004) and to come closer to the length scales in climate model studies, we chose to use a relatively large horizontal domain of 1024 km × 1024 km (larger than a typical climate model grid box) with a horizontal resolution of 4 km. We also performed a pair of higher-resolution simulations (2 km) to test the robustness of our results; future modeling studies at a range of resolutions and domain sizes are desirable.

The model uses periodic lateral boundaries, and a rigid lid at the top of the domain. All simulations use a 64-level vertical grid (capped at 27 km) with the first level at 37.5 m and grid spacing gradually increasing from 80 m near the surface to 400 m above 5 km, and a variable time step (10 s or less to satisfy the Courant–Friedrichs–Lewy condition). To reduce gravity wave reflection and buildup, Newtonian damping is applied to all prognostic variables in the upper third of the model domain. The wind is relaxed over a time scale of 2 h toward a background wind profile with vertical shear. The background wind profile has a value of 5 m s^{-1} in the x direction at the surface, and decreases linearly in z to 16 km, above which it is identically zero.

We analyze two main simulations: a control simulation with an SST of 300 K, and a warmer simulation with an SST of 305 K. The CRM is run in each case to statistical radiative–convective equilibrium using specified radiative cooling. The radiative cooling rates used are the temporally and horizontally averaged radiative cooling rates as a function of height in a simulation with corresponding SSTs (300 and 305 K) on a smaller domain (64 km × 64 km horizontal domain with 1-km resolution). The smaller domain simulations are run with fully interactive longwave and shortwave radiation. An additional simulation was performed in which the radiative
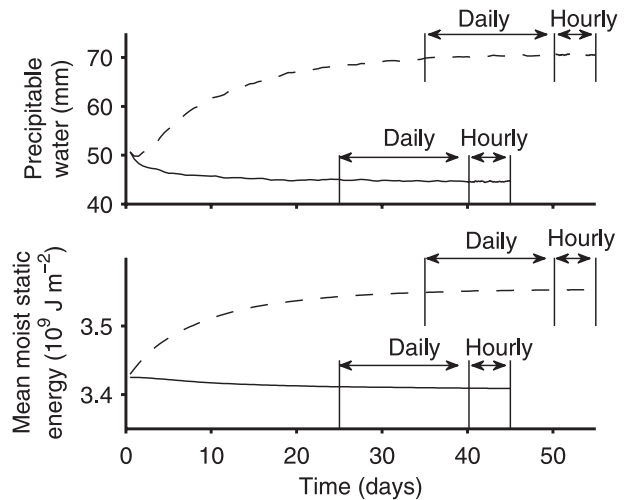

FIG. 1. Domain mean column water vapor and moist static energy as a function of time in the control (solid) and warm (dashed) simulations. Radiative–convective equilibrium is taken to have been reached after 25 (35) days in the control (warm) simulation. Once equilibrium is reached, we start our analysis of precipitation extremes at daily time scales for 15 days, and at hourly time scales for 5 days.

cooling rate from the small-domain simulation with SST of 300 K is applied to a large-domain 305-K simulation in order to assess the effects of holding the radiative cooling rate unchanged (the "fixed radiation" simulation; section 5).

Precipitation rates, vertical velocities, and all other variables studied are model gridpoint variables. Precipitation extremes are defined as high percentiles of the surface precipitation rate, including all grid points (wet and dry). Once equilibrium is reached, we start our analysis of precipitation extremes at daily and hourly time scales (Fig. 1). More precisely, for the 300-K SST simulation, radiative-convective equilibrium is taken to have been reached in 25 days; then daily mean statistics are collected between day 25 and day 40, and hourly mean statistics are collected between day 40 and day 45. Similarly, for the 305-K SST simulation, radiative-convective equilibrium is taken to have been reached in 35 days; then daily mean statistics are collected between day 35 and day 50, and hourly mean statistics are collected between day 50 and day 55.

3. Changes in precipitation extremes

Before quantifying the changes in precipitation percentiles with warming, in Fig. 2 we show a composite of conditions associated with strongly precipitating events in the 300-K SST simulation (the other simulation with an SST of 305 K has the same general features). The figure shows composites centered at points with gridbox

Non–precipitating condensate (g kg^{-1})

Vertical velocity w (m s^{-1})

Precipitation (mm day^{-1})

Cross section across shear   Cross section along shear (arrows)
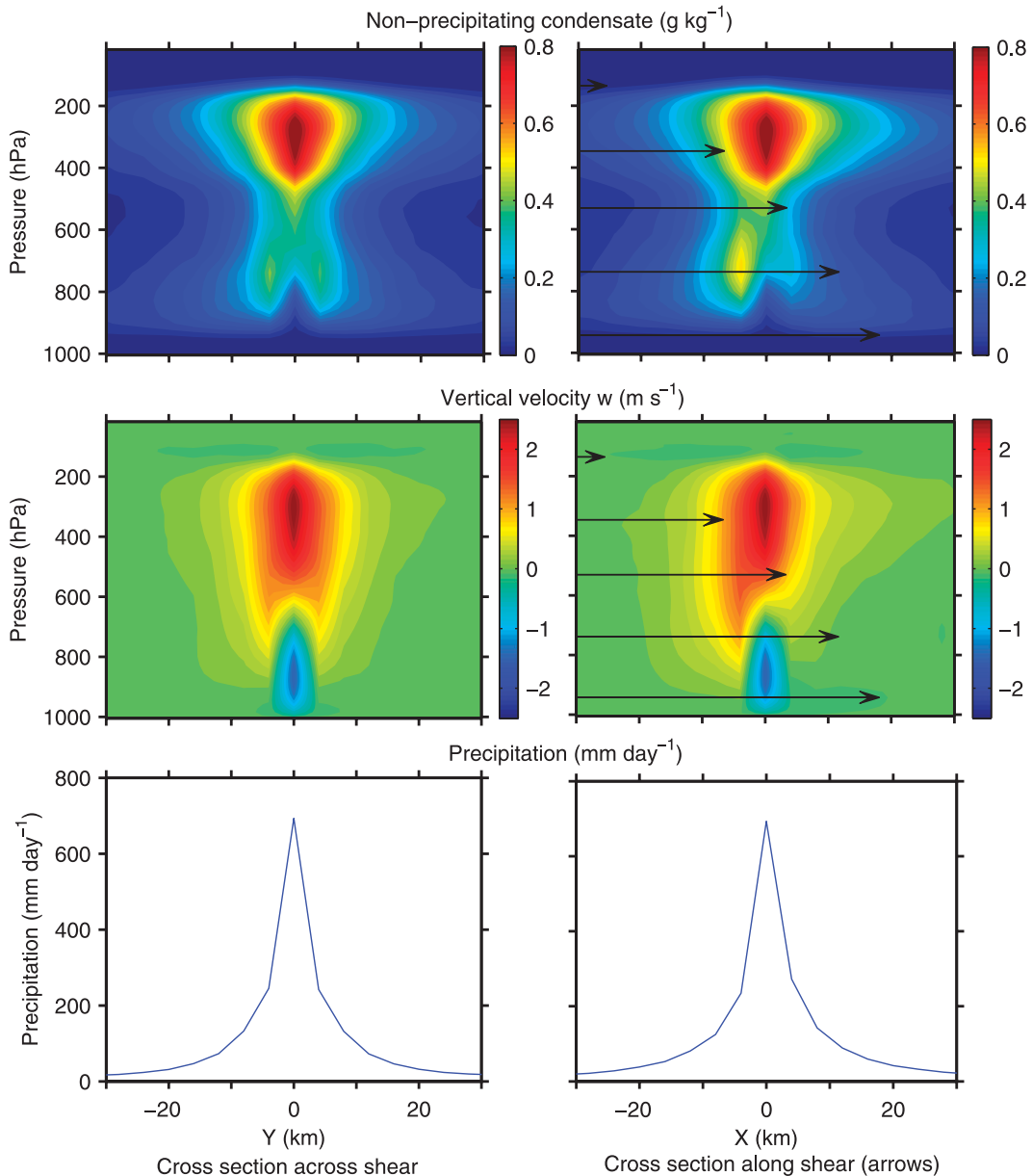
FIG. 2. Composite centered at points with precipitation above the 99.9th percentile of the precipitation distribution in the 300-K SST simulation. Here, precipitation is the instantaneous gridbox precipitation, and its distribution is computed using all points, dry and wet. The instantaneous nonprecipitating condensates, vertical velocities, and precipitation rates at times and places of extreme precipitation are shown: (left) in the along-shear direction and (right) in the across-shear direction; the background shear is indicated with black arrows scaled such that the bottom arrow represents a horizontal velocity of 5 m s^{-1} (the background velocity decreases linearly in z from 5 m s^{-1} at the surface to 0 m s^{-1} at $z = 16$ km, above which it is set to 0 m s^{-1}). All quantities shown in the figure have been interpolated to pressure levels.

precipitation above the 99.9th precipitation percentile. All fields shown are instantaneous in time, so that Fig. 2 shows a composite of instantaneous snapshots at times and places with strong precipitation.

Strong precipitation is associated with strong upward motion and cloudiness in middle to high levels, as well as

strong downdrafts at low levels driven by the evapora-tion of precipitating condensates. Note that while the instantaneous vertical velocity conditioned on the 99.9th precipitation percentile is about 2 m s^{-1}, the maximum instantaneous upward velocity can reach values as large as 40 m s^{-1} [the distribution of w is similar to the one
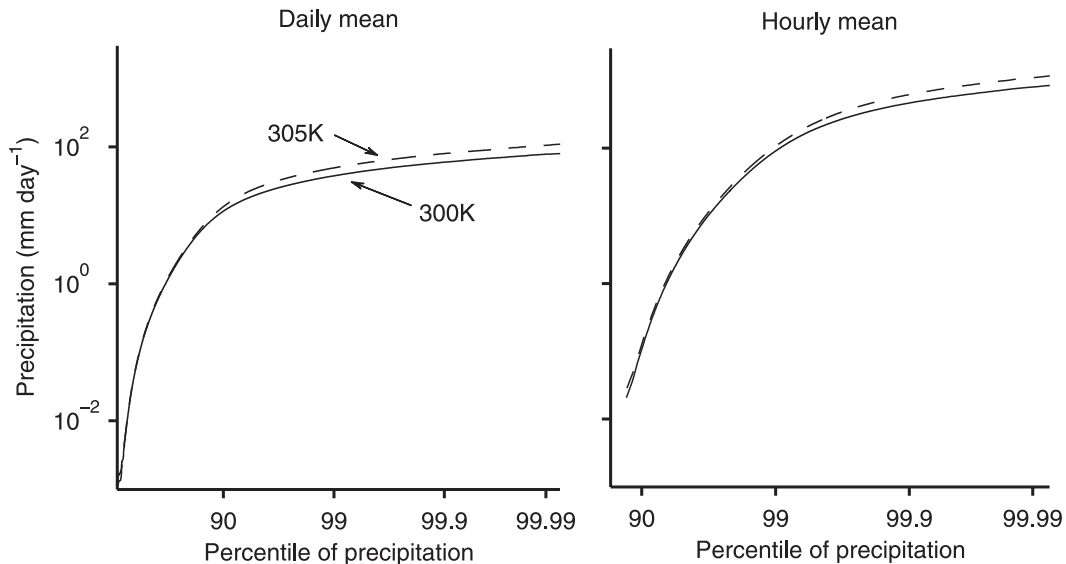
FIG. 3. Cumulative distribution functions of daily and hourly mean precipitation rates in the control 300-K SST simulation (solid) and warm 305-K SST simulation (dashed).

given in Pauluis and Garner (2006) for the same spatial resolution]. Figure 2 shows an asymmetry in the along-shear direction (aligned with x), with preferred upward motion and cloudiness upwind. This is due to the enhancement of convergence upwind, as the outflow from downdrafts encounters air with greater momentum in the positive x direction at low levels. A similar phenomenon has been observed in the context of mesoscale precipitation features (Leary and Houze 1979). Our simulations exhibit a limited organization in the along-shear direction into long-lived precipitating systems that propagate through the domain at close to the background surface velocity $U = 5$ m s^{-1}.

Daily and hourly precipitation rates as a function of percentile in the control and warm simulations are shown in Fig. 3. We see that warming generally yields larger precipitation rates. To make clearer the rate of increase at different percentiles, in Fig. 4 we show the ratio (warm simulation over control simulation) of the precipitation rates as a function of precipitation percentile. This ratio is everywhere above unity, implying that the intensity of precipitation increases at all percentiles when SST is increased. The frequency of precipitation hardly changes ($<0.1\%$ K^{-1}) so that the mean precipitation must increase. The fractional rate of increase in mean precipitation (4%–5% K^{-1}) is somewhat larger than that of global mean precipitation in climate model simulations driven by increased greenhouse gas concentrations ($\sim2\%$ K^{-1}). One contribution to the difference is that we increase SST but do not change the CO_2 concentrations (although water vapor concentrations

do increase), but shortwave radiation changes and ocean heat uptake also contribute to changes in the energy budgets of climate model simulations (Stephens and Ellis 2008).

Another important feature of the precipitation changes shown in Fig. 4 is that the ratio of precipitation rates asymptotes at the highest percentiles, and that the asymptotic value is similar at daily and hourly time scales, 7.3% and 7.6% K^{-1}, respectively (see also Table 1). The asymptotic value is close (but not equal) to the rate of increase in surface water vapor ($\approx8\%$ K^{-1}; see Fig. 4 and Table 1), and substantially lower than the rate of increase in column water vapor ($\approx11.5\%$ K^{-1}). It is not much greater than the fractional rate of increase in mean precipitation (4%–5% K^{-1}). But as discussed in section 5, the rates of change of mean and extreme precipitation are subject to different constraints and can be quite different in general.

4. Precipitation extremes scaling based on dry static energy budget

a. Derivation of expression for precipitation rate in extreme events

We wish to relate precipitation extreme changes to changes in dynamic, thermodynamic, and microphysical variables. To do this, we first derive an expression for the precipitation rate in an extreme precipitation event. We then use this expression to diagnose the different contributions to the scaling behavior of precipitation extremes, and to determine in which circumstances precipitation extremes might be expected to scale with the amount of
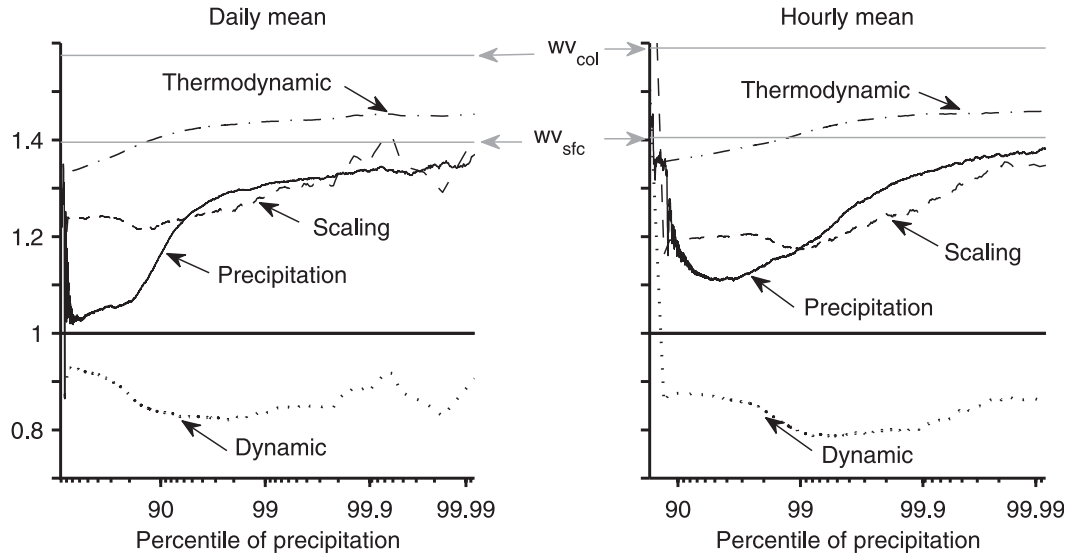
FIG. 4. Ratio (warm simulation over control simulation) of the precipitation rate and precipitation extremes scalings as a function of precipitation percentile, at daily and hourly time scales. The scaling (dashed), thermodynamic scaling (dash-dotted), and dynamic scaling (dotted) are shown. The thermodynamic scaling neglects changes in vertical velocity, and the dynamic scaling neglects changes in temperature. The changes in atmospheric column water vapor wv_{col} and in surface water vapor wv_{sfc} are indicated with horizontal gray lines.

water vapor. We use an energy rather than a water budget because an energy budget allows us to more easily define a thermodynamic component (with no dependence on relative humidity), and also because the weak horizontal gradients of temperature in the tropics help to eliminate horizontal advective terms. Following the approximate thermodynamic formulation of the model (Khairoutdinov and Randall (2003), a vertically integrated dry static energy (DSE) budget may be written as

$$\left[\frac{Ds}{Dt}\right] \approx L_v\left[\frac{D(q_r + q_c)}{Dt}\right] + L_s\left[\frac{D(q_s + q_g + q_i)}{Dt}\right] + L_v P, \tag{1}$$

where the Lagrangian derivative is given by

$$\frac{D}{Dt} = \frac{\partial}{\partial t} + u_i\frac{\partial}{\partial x_i}$$

and the mass-weighted vertical integral is given by

$$[\cdots] = \int_{surface}^{100\,hPa} (\cdots)\overline{\rho}\, dz.$$

In the above equations, $s = c_p T + gz$ denotes dry static energy; q_r rain mixing ratio; q_c is cloud liquid water mixing ratio; q_s is snow mixing ratio; q_g is graupel mixing ratio; q_i is cloud ice mixing ratio; L_v and L_s are latent heats of evaporation and sublimation, respectively; P is

surface precipitation; $\overline{\rho}(z)$ is the mean density profile; and u_i ($i = 1, 2, 3$) are the resolved wind speeds along the Cartesian directions x, y, and z, respectively. In (1), there is only liquid precipitation at the surface because our SSTs are too warm for graupel or snow surface precipitation. Consistent with the CRM, we neglect water contributions to the heat capacity and the temperature dependencies of L_s and L_v. Since we are interested in

TABLE 1. Fractional changes in mean precipitation, precipitation extremes (99th, 99.9th and 99.99th percentiles), mean column water vapor, mean surface mixing ratio, mean saturation column water vapor, mean surface saturation mixing ratio, and precipitation efficiency ϵ (at the 99th, 99.9th and 99.99th precipitation percentiles) between the control simulation (SST = 300 K) and the warm simulation (SST = 305 K). Fractional changes are normalized by the SST change to give results in % K^{-1}. Mean quantities are averaged in space and time.

	Daily (% K^{-1})	Hourly (% K^{-1})
Mean precipitation	4.0	4.9
99th precipitation percentile	6.1	3.5
99.9th precipitation percentile	6.7	6.6
99.99th precipitation percentile	7.4	7.6
Column water vapor	11.5	11.8
Saturation column water vapor	10.9	11.0
Surface mixing ratio	7.9	8.1
Saturation surface mixing ratio	7.5	7.5
ϵ at 99th precipitation percentile	0.4	0.04
ϵ at 99.9th precipitation percentile	−0.3	1.1
ϵ at 99.99th precipitation percentile	−0.7	0.5

precipitation extremes, we neglect subgrid-scale fluxes as well as the radiative cooling term in (1), which are negligible compared to the other terms when strong precipitation occurs. The upper boundary for the vertical integral is introduced to exclude the top layers of the model where damping is applied to avoid gravity wave reflection and build up; we conducted the same analysis changing the upper boundary to 150 hPa and found that our results are not sensitive to this value.

Where and when strong surface precipitation occurs, the time derivative of dry static energy is well approximated by the vertical advection term $Ds/Dt \approx w \partial s/\partial z$ (less than 0.5% error at hourly time scales and less than 2% error at daily time scales at the 99.99th precipitation percentile). This simplification occurs because of the strong upward motions associated with precipitation extremes and the weak horizontal gradients of temperature in the tropics. The weak temperature gradients also allow us to approximate the dry static energy by its horizontal and time mean profile $s(z)$. If we also make the hydrostatic approximation, and assume that the mean atmospheric lapse rate is close to moist adiabatic (a fairly good approximation in the model above the boundary layer), then $ds = c_p dT + g dz \simeq -L_v dq_{\text{sat}}$, where q_{sat} denotes saturation mixing ratio, and we have neglected the difference between L_v and L_s for the purpose of deriving a simple approximate expression. Equation (1) then becomes

$$ P_e \approx -\left[w \frac{\partial q_{\text{sat}}}{\partial z} \right] - \left[\frac{D(q_r + q_c + q_s + q_g + q_i)}{Dt} \right], \quad (2) $$

where the precipitation rate in an extreme event is denoted P_e. We now define a precipitation efficiency ϵ such that the precipitation rate in an extreme event can be written simply as

$$ P_e = -\epsilon \left[w \frac{\partial q_{\text{sat}}}{\partial z} \right]. \quad (3) $$

To the extent that the approximations made so far are accurate, the precipitation efficiency will be equal to one plus the ratio of the two terms on the right-hand side of (2). Expression (3) for the precipitation rate was derived from an energy budget, but it resembles a water budget and can be interpreted as such: $-[w \partial q_{\text{sat}}/\partial z]$ represents the total net condensation (and deposition) in the atmospheric column, including condensation from upward motion as well as evaporation of precipitating, and nonprecipitating condensates maintaining a moist adiabatic lapse rate in downdraft regions. Only a fraction of the net condensation precipitates out at the surface. In the limit $\epsilon = 1$ all the net condensates precipitate out; in the limit $\epsilon = 0$, all condensates are advected from the column or

build up in the column over the time scale in question. Because the precipitation efficiency relates to the net condensation (condensation − evaporation), it differs from the more conventional precipitation efficiency based on the ratio of the precipitation rate to the condensation rate. At hourly time scales both advection and the time rate of change of condensates are important for the precipitation efficiency, whereas at daily time scales only the horizontal advection from the column is important.

Expression (3) can be used to relate changes in precipitation extremes to changes in the dynamics through the vertical velocity, to changes in the thermodynamics through the vertical rate of change of saturation mixing ratio, and to changes in condensate transports through the precipitation efficiency. It is similar to previous expressions for precipitation extremes (Iribarne and Godson 1981; O'Gorman and Schneider 2009a; Sugiyama et al. 2010), except that the vertical velocity is now at the convective scale, and there is an additional factor involving ϵ.

b. Contributions to changes in precipitation extremes in the CRM simulations

We now investigate the contributions to the changes in precipitation extremes in response to warming. The precipitation efficiency was evaluated based on (3) in terms of the diagnosed precipitation rates at a given high percentile, the conditional mean of the vertical velocity at that precipitation percentile, and using the horizontal and time mean of the saturation mixing ratio.[1] The precipitation efficiency has a value at high precipitation percentiles of about 80% at daily time scales and 70% at hourly time scales, and it remains approximately constant between the control and warm simulations in the CRM (see Table 1). If changes in the precipitation efficiency are neglected, then fractional changes in P_e are given by the scaling relation:

$$ \frac{\delta P_e}{P_e} \approx \frac{\delta [w \partial q_{\text{sat}}/\partial z]}{[w \partial q_{\text{sat}}/\partial z]}. \quad (4) $$

We call this a scaling because it only approximately predicts the fractional changes in precipitation extremes with warming, but not their magnitude in a given simulation. We can further decompose it as

$$ \frac{\delta P_e}{P_e} \approx \frac{[w \delta(\partial q_{\text{sat}}/\partial z)]}{[w \partial q_{\text{sat}}/\partial z]} + \frac{[\delta(w) \partial q_{\text{sat}}/\partial z]}{[w \partial q_{\text{sat}}/\partial z]}, \quad (5) $$

---

[1] It is important to note that the precipitation efficiency is defined and evaluated in terms of (3), so that it potentially includes contributions from the approximations used in deriving (2), in addition to the contribution from the difference between the surface precipitation rate and the column-integrated net condensation rate.
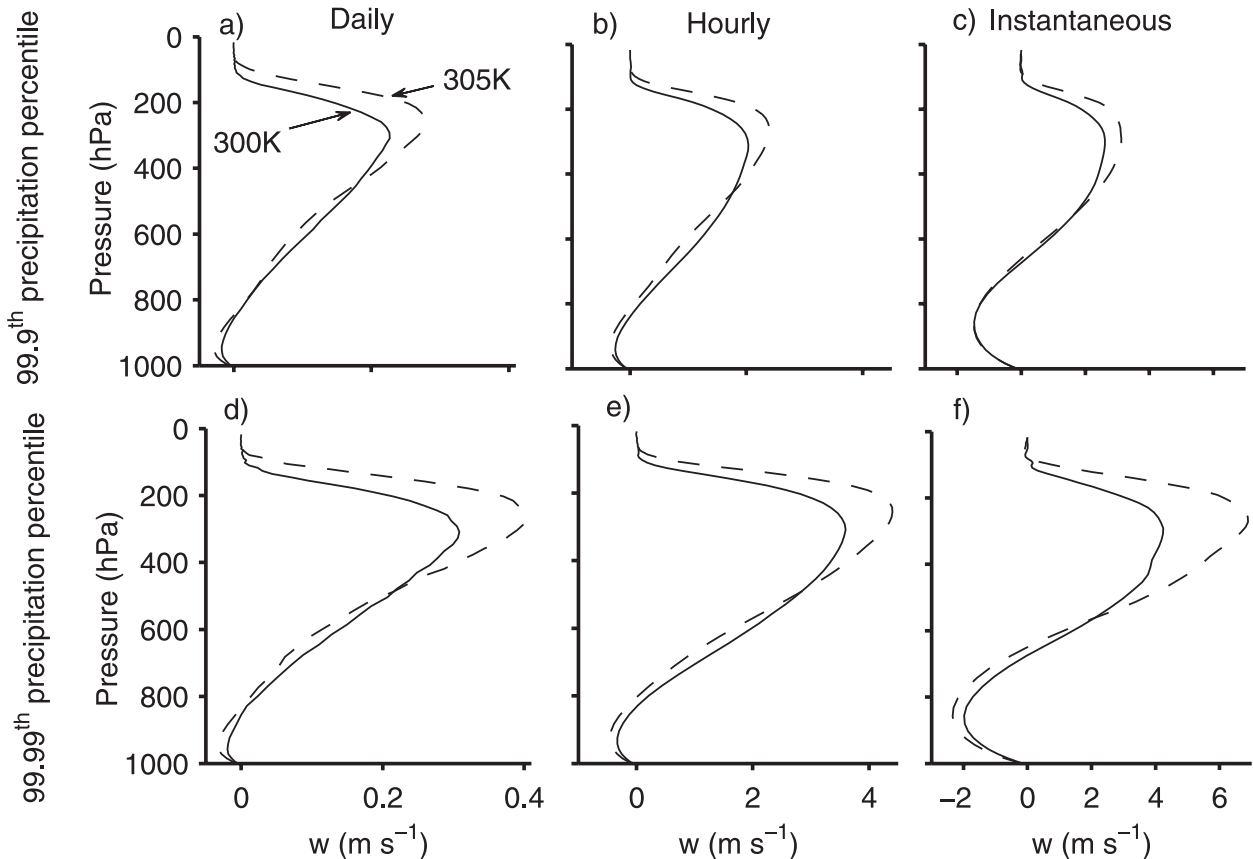
FIG. 5. (a)–(c) Composites of the vertical velocity w at points with precipitation exceeding the 99.9th precipitation percentile and (d)–(f) at points with precipitation exceeding the 99.99th. The composites are made by averaging the vertical profile of w over all points with precipitation exceeding the given percentile. Results are shown for (a),(d) daily mean, (b),(e) hourly mean, and (c),(f) instantaneous w and precipitation. The solid lines show results for the 300-K SST control simulation and the dashed lines show results for the 305-K SST warm simulation.

which is the sum of a thermodynamic scaling $[w\delta(\partial q_{sat}/\partial z)]/[w\partial q_{sat}/\partial z]$ and a dynamic scaling $[\delta(w)\partial q_{sat}/\partial z]/[w\partial q_{sat}/\partial z]$. The thermodynamic scaling only accounts for changes in the thermodynamics (through changes in the saturation mixing ratio), and is particularly useful in so far as it relates the intensity of precipitation extremes to the vertical profile of the mean saturation mixing ratio, which only depends on temperature and pressure. The dynamic scaling only accounts for changes in circulation strength (through changes in vertical velocities). Similar decompositions of changes in precipitation extremes into thermodynamic and dynamic components have been made previously (Emori and Brown 2005; O'Gorman and Schneider 2009a,b). Note that the dynamic scaling depends on a $\partial q_{sat}/\partial z$-weighted integral of w, rather than, say, the vertical velocity at 500 hPa. The full, thermodynamic, and dynamic scalings are shown in Fig. 4 and are computed using the conditional mean of the vertical velocity at a given precipitation percentile,

and using the horizontal and time mean of the saturation mixing ratio. The full scaling (4) predicts an increase of roughly 7% K^{-1} in precipitation extremes, both at hourly and daily time scales. The thermodynamic scaling yields an increase of about 9% K^{-1}, which slightly overestimates the change in precipitation extremes, and is offset by the decrease found in the dynamic scaling. The close agreement between the scaling (4) and the diagnosed changes in daily precipitation extremes implies relatively small changes in precipitation efficiency. The agreement is slightly weaker at hourly time scales, but this is due to the use of the global mean q_{sat} when evaluating the scaling (4); if instead q_{sat} conditioned on precipitation extremes is used, the agreement is very close, implying a small change in precipitation efficiency.

Although there is an increase in the maximum (over the column) of the vertical velocity conditioned on precipitation extremes (Fig. 5), changes in the vertical velocity slightly reduce the magnitude of precipitation

extremes. The reduction occurs because the important dynamical quantity for precipitation extremes is the $\partial q_{sat}/\partial z$-weighted integral of w. Here, w generally increases and shifts upward, but it decreases in the lower troposphere where the magnitude of $\partial q_{sat}/\partial z$ is large. The reduction in the vertical velocity at low levels (conditioned on precipitation extremes) partially arises from an increase in the magnitude of downdrafts. Our results suggest that estimates of the dynamical contribution to changes in precipitation extremes in terms of vertical velocities at a specific level (e.g., 500 hPa) will generally not be accurate. The sensitivity to the profile of vertical velocity is consistent with the GCM study of Sugiyama et al. (2010) who found that both the amplitude and the vertical profile of vertical motion affect precipitation extremes, although our vertical velocity is now at the convective scale. The increase and upward shift of the maximum of the vertical velocity occurs not only for the vertical velocity conditioned on precipitation extremes, but also more generally, and will be discussed in more detail in section 6.

It has become common to phrase changes in precipitation rates in terms of changes in the amount of atmospheric water vapor (e.g., Held and Soden 2006; Pall et al.2007; Allan and Soden 2008), with ambiguity in some cases as to whether column or surface water vapor is relevant. Following O'Gorman and Schneider (2009a,b), we can use the thermodynamic scaling to address this issue, since the thermodynamic scaling captures much of the behavior of the simulated precipitation extremes. If we further assume a constant vertical velocity in the vertical (with convergence and divergence concentrated only at the surface and upper limit of integration), then

$$
\begin{aligned}
\delta P_e &\approx -\int w\,\delta\!\left(\frac{\partial q_{sat}}{\partial z}\right)\!\rho\,dz \\
&\approx -w(500\ \text{hPa})\rho_0\,\delta\!\left(\int \frac{\partial q_{sat}}{\partial z}\,dz\right) \\
&\approx w(500\ \text{hPa})\rho_0\,\delta q_{sat}^{sfc},
\end{aligned}
\tag{6}
$$

where ρ_0 is a reference density, q_{sat}^{sfc} is the saturation mixing ratio at the surface, and we have neglected the saturation mixing ratio at the tropopause. The preceding discussion makes clear that this is only a rough approximation, since the thermodynamic scaling neglects changes in precipitation efficiency and in vertical velocities, and in addition we have neglected the vertical variations in w seen in Fig. 5. It indicates that the fractional change in precipitation extremes is given by

$$
\frac{\delta P_e}{P_e} \approx \frac{\delta q_{sat}^{sfc}}{q_{sat}^{sfc}},
\tag{7}
$$

so that precipitation extremes are expected to more closely follow surface rather than column integrated water vapor, as observed in the CRM (Fig. 4). In the tropics, using column water vapor as a proxy for the rate of change of precipitation extremes instead of surface humidity can lead to substantial overestimates. O'Gorman and Muller (2010) found that for climate model simulations of the A1B emissions scenario, the multimodel mean rate of increase in zonal mean column water vapor is 8.4% K^{-1} at the equator, whereas the increase in surface specific humidity is only 5.8% K^{-1}, yielding an overestimate of about 45%. In our CRM simulations, the fractional rates of increases in column and surface water vapor are larger because of the greater temperature change ($\sim$12% and 8% K^{-1}, respectively, see Table 1), but they have a similar ratio.

c. Sensitivity to the spatial resolution

Our simulations can be used to investigate to some extent how spatial resolution impacts the changes in precipitation extremes with warming. This is important both for trying to relate our results to GCM studies with much larger grid spacings (of order 100 km), and for assessing how changes in the convective-scale dynamics in our simulations might be affected by finite spatial resolution. The link to GCM simulations is, of course, greatly complicated by the lack of large-scale circulations in our simulations. Figure 6 shows the amplification of precipitation extremes at various resolutions. Statistics at 2 km were obtained from new simulations with twice the resolution and half the domain size. Statistics at 16 and 24 km were obtained by coarsening the outputs from the original simulation at 4-km resolution (the coarsening is simply obtained by taking spatial averages). The actual value of precipitation at a given percentile is sensitive to the resolution (not shown), with weaker rainfall rates as more averaging is applied; but the amplification of high precipitation percentiles with warming is robust to the resolution, with a consistent increase of 7.5%–8% K^{-1}. In the 2-km-resolution simulations, a slightly greater increase in precipitation efficiency is implied at hourly time scales than at the original spatial resolution, but this is mostly due to the use of the global mean q_{sat} when evaluating the scaling (4); if instead q_{sat} conditioned on precipitation extremes is used, the agreement is closer and implies only a slight increase in precipitation efficiency. As before, the approximate scaling of precipitation extremes with surface water vapor concentration in each case results primarily from a partial cancellation of changes in the contributions from the dynamics (weakening) and thermodynamics (strengthening).
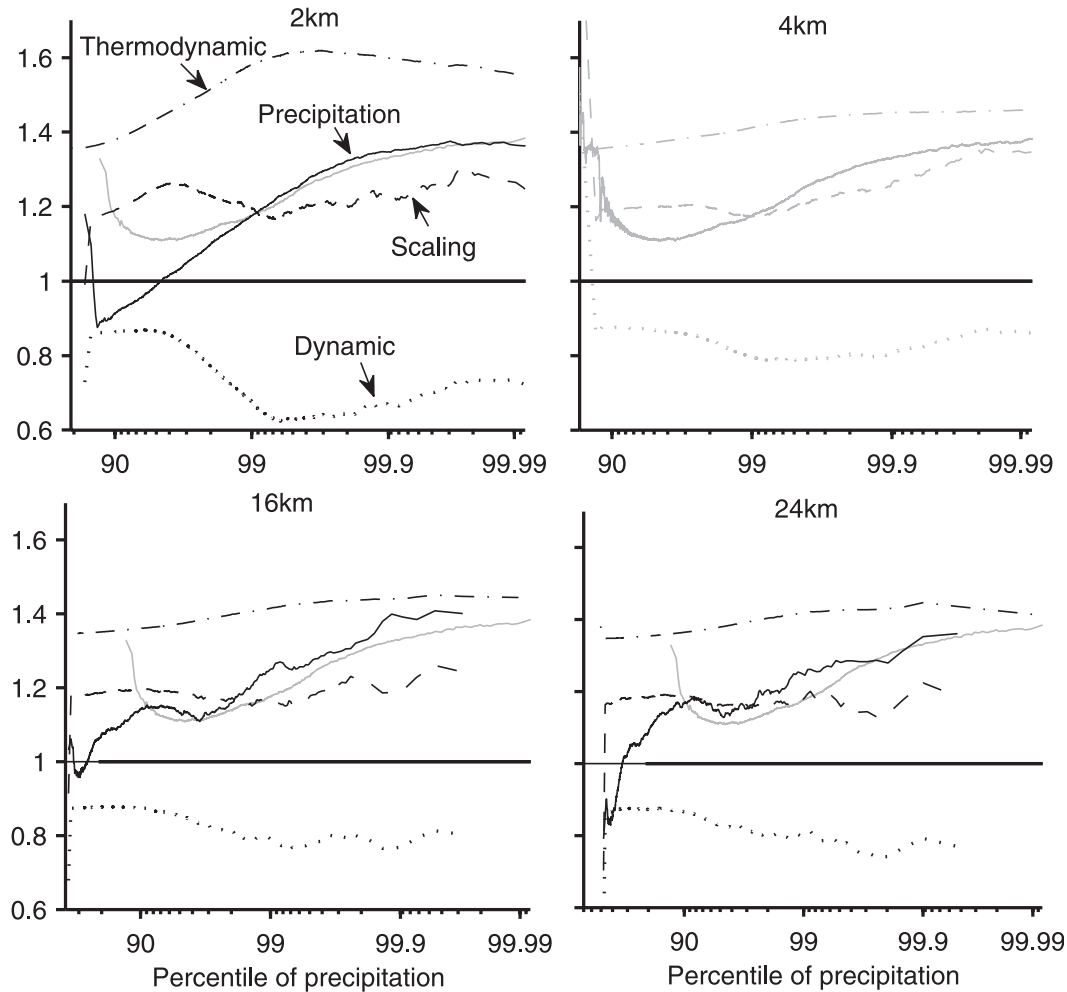
FIG. 6. Changes in hourly precipitation rates as in Fig. 4, but at different spatial resolutions. The 16- and 24-km resolution results are obtained by spatial averaging of the precipitation rates in the 4-km grid simulations, while the 2-km resolution results are based on an additional pair of simulations with a 2-km grid. The ratio curves at the original resolution (4 km reproduced from Fig. 4) are shown in light gray for comparison (the 4-km precipitation ratio curve is also added to each panel to make comparison easier). The curves become noisier as the resolution increases (because of the lack of data), but overall one can see that the amplification of high precipitation percentiles with warming is robust to the resolution changes, with a consistent increase of 7.5%–8% K^{-1}. The change in the thermodynamic scaling is somewhat larger at 2-km resolution; this is due to a change in the vertical profile of vertical velocity $w(z)$ in the control run when resolution is increased; at 2-km resolution, $w(z)$ is stronger in the upper troposphere where the amplification of $\partial qs/\partial z$ is largest, yielding a larger thermodynamic contribution.

5. Sensitivity to the radiative cooling profile

Both mean and extreme precipitation increase substantially between the control and warm simulations, albeit at different fractional rates of change. To investigate how the changes in mean precipitation relate to changes in precipitation extremes, we conduct a second 305-K SST simulation, but with the same imposed radiative cooling profile as the control 300-K SST simulation; we will refer to this alternative warm simulation as the fixed-radiation simulation.

The radiative cooling profile strongly influences the mean precipitation rate because of energetic constraints. For example, the increase in mean precipitation between the control and warm simulation can be understood through the mean energy budget of the atmosphere $L_v P + S \approx Q_{rad}$, where $L_v P$ is the latent heating, S is the surface sensible heat flux, and Q_{rad} is the vertically integrated radiative cooling. The increase in the mean precipitation rate ($\Delta L_v P \approx +20$ W m^{-2}) is therefore directly related to the increase in radiative cooling ($\Delta Q_{rad} = +16.4$ W m^{-2}) and a slight reduction in sensible heat flux ($\Delta S \approx -1.5$ W m^{-2}).
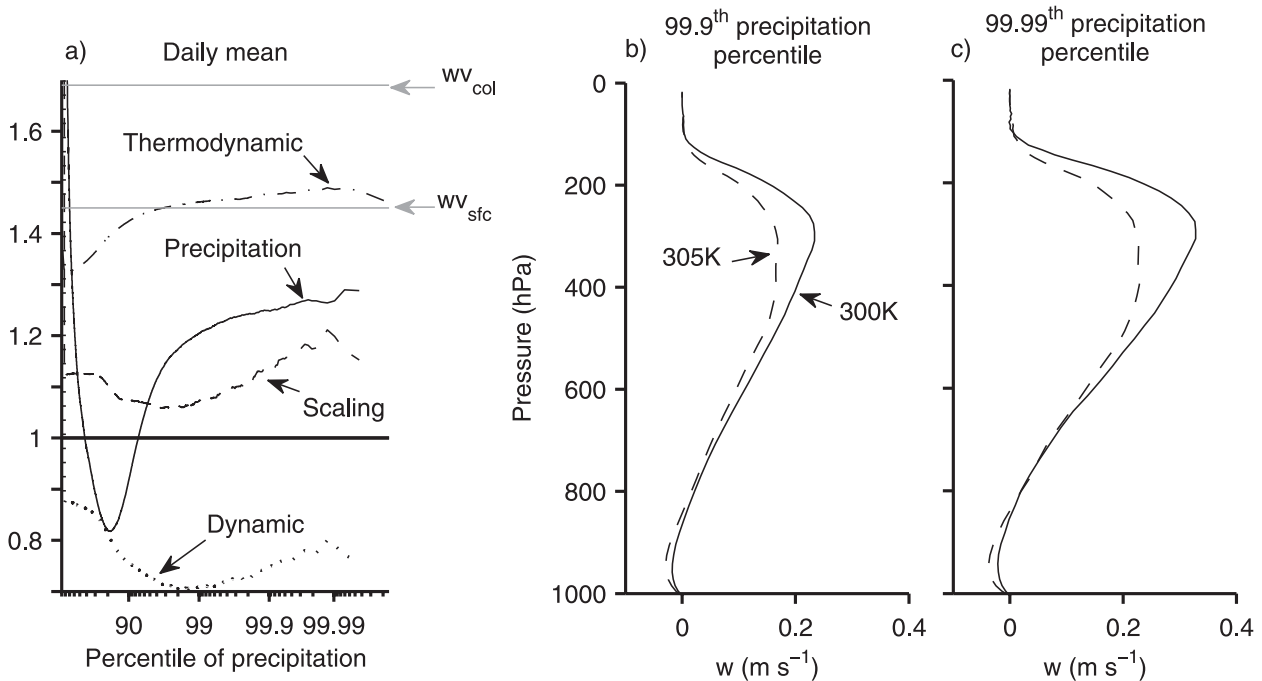
FIG. 7. Changes in precipitation extremes and vertical velocities between the control and fixed-radiation simulations (these simulations have the same radiative cooling profile but different SST). (a) The ratio (fixed-radiation simulation over control simulation) of the daily precipitation rate as a function of precipitation percentile; the scalings (6) and its thermodynamic and dynamic contributions are also shown, as well as the increase in surface and atmospheric water vapor. Composites of the daily mean vertical velocity w (b) at points with daily precipitation exceeding the 99.9th percentile and (c) at points with daily precipitation exceeding the 99.99th percentile. In (b) and (c), the solid lines show results for the control simulation and the dashed lines show results for the fixed-radiation simulation.

Similarly, from the energy budget we expect the mean precipitation to be roughly the same in the control and fixed-radiation simulations. This is approximately true, with $\Delta Q_{\mathrm{rad}} \equiv 0$ W m^{-2} by definition, $\Delta S \approx -2.4$ W m^{-2} and $\Delta L_v P \approx +4$ W m^{-2}. The fractional rate of change of mean precipitation is less than 0.8% K^{-1} (cf. 4%–5% K^{-1} for the control to warm simulation). But precipitation extremes still increase by a large amount, 5.6% K^{-1} (Fig. 7). Thus, holding the radiative profile fixed almost completely eliminates the increase in mean precipitation, but only reduces the increase in precipitation extremes by 23%. This gives us confidence that changes in precipitation extremes are only weakly affected by global energetics, and are largely determined by local processes. We next quantify the changes in precipitation extremes in the fixed-radiation simulation in more detail.

a. Impact of holding radiative cooling fixed on precipitation extremes

The ratio of daily precipitation rates (warm fixed-radiation simulation over control simulation) as a function of precipitation percentiles is shown in Fig. 7, along with the precipitation extremes scaling (6) and its dynamic and thermodynamic components. In this case, the ratio is not above unity at all percentiles; it is less than 1

for 35% of the points, contributing 40% (35%) of the total precipitation in the control (fixed radiation) simulation. Because the mean precipitation is constrained by energetics, while high percentiles of precipitation increase consistent with the thermodynamics, one might expect the distribution of precipitation to rearrange so that it rains less often, but more intensely. In other words, the intensity would go up and the frequency would go down, keeping the mean constant. But this is not the case here: the frequency does not change (<0.7% K^{-1} increase) and the low percentiles decrease, while the high percentiles increase.

The increase in precipitation extremes still converges at the highest percentiles, to about 5.6% K^{-1}. The prediction from the scaling (4) is not as accurate as before at daily time scales because of an increase in ϵ (from 80% to about 90% at high percentiles of daily precipitation).[2] The increase in precipitation efficiency is offset to some

---

[2] We have confirmed that the implied increase in precipitation efficiency is not simply an artifact of the simplifying assumptions in our scaling derivation [$ds \simeq -L_v dq_{\mathrm{sat}}$ and using the global mean q_{sat} in the scaling (4)], although these assumptions do make some contribution to the discrepancy between changes in the scaling and the precipitation extremes.
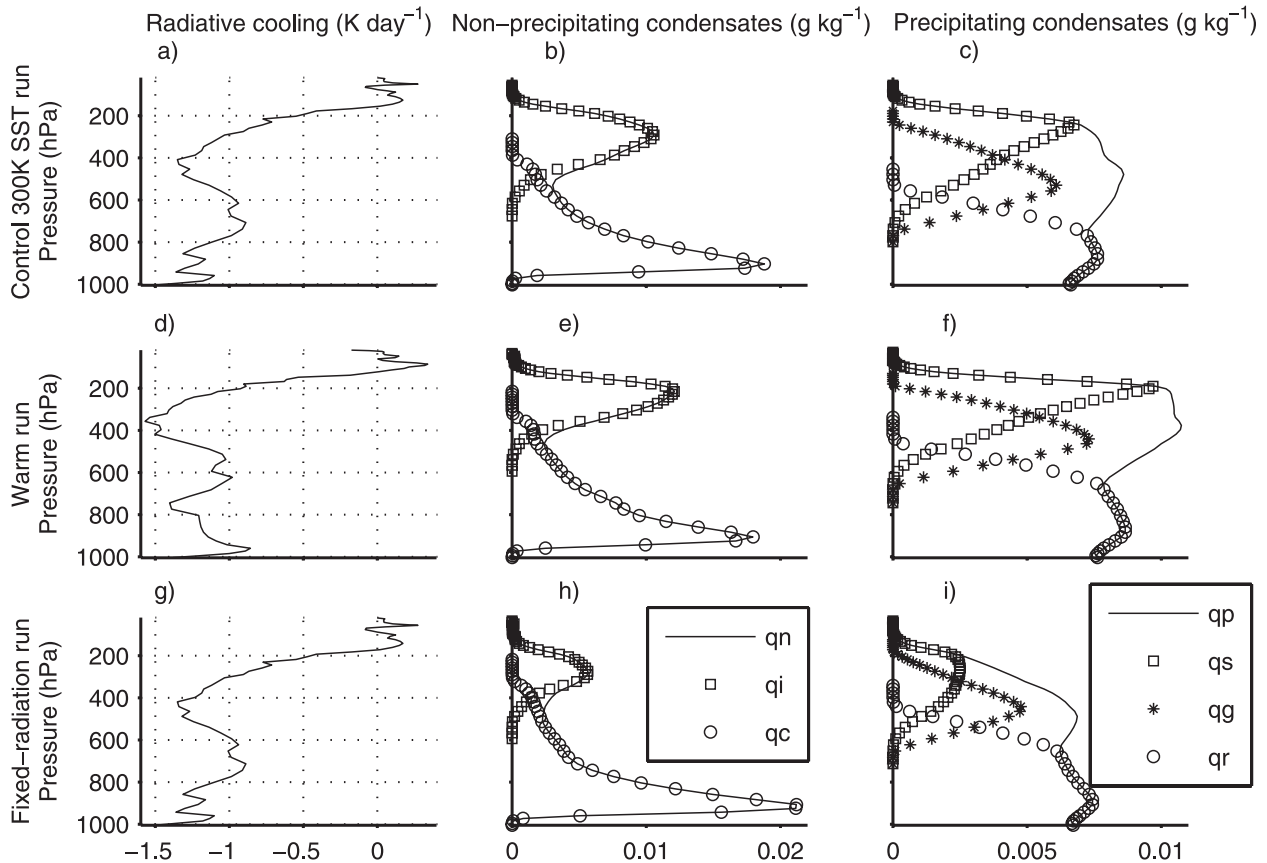
FIG. 8. Radiative cooling profiles, and domain mean condensate distributions in (a)–(c) the control 300-K SST simulation, (d)–(f) the warm simulation, and (g)–(i) the fixed-radiation simulation. (d),(g) The warm and fixed-radiation simulations have the same SST of 305 K but different radiative cooling profiles, and the resulting horizontal and time mean condensate profiles are very different in the upper troposphere. (b),(e),(h) The mean nonprecipitating condensates mixing ratio $q_n = q_i + q_c$ is shown, where q_i denotes cloud ice and q_c denotes cloud liquid water. (c),(f),(i) The mean precipitating condensates mixing ratio $q_p = q_s + q_g + q_r$ is shown, where q_s denotes snow, q_g graupel, and q_r liquid rain.

extent by a decrease in vertical velocities at all levels (Fig. 7). As before, changes in precipitation extremes are closer to the fractional changes in surface humidity (9.0% K^{-1}) than column water vapor (13.8% K^{-1}). We next discuss a possible cause for the different behavior of the precipitation efficiency when the radiative cooling is held fixed, followed by the controls on vertical velocities in general in section 6.

b. Impact of holding radiative cooling fixed on condensates

The major impact of holding the radiative profile fixed is on the condensate amounts at upper levels (Fig. 8), with much less condensates in the fixed-radiation (305 K) simulation compared with the standard warm (305 K) simulation. In the fixed-radiation simulation, the rapid decay of the radiative cooling around 200 hPa controls the average cloud-top height (Hartmann and Larson 2002; Kuang and Hartmann 2007), resulting in

higher cloud mean temperatures than in the standard 305-K simulation. This has a direct impact on the partition of hydrometeors, since in this model the total precipitating condensate amount is partitioned into rain, graupel, and snow with a partition function that depends only on temperature. Increased cloud temperatures lead to larger graupel-to-snow and rain-to-snow ratios, with faster terminal velocities, which together with the lower updraft velocities yields lower concentrations of condensates in the clouds. An increase with warming in terminal velocities and the amount of graupel at certain levels has also been discussed by Del Genio (2003).

The control and standard warm simulations have almost the same amount of nonprecipitating condensates (the domain mean liquid and ice cloud content increased by a modest 0.3% K^{-1}). But between the control simulation and the fixed-radiation simulation, the domain mean liquid and ice cloud content decreases by -3.5% K^{-1}, mainly due to a decrease in the amount of ice. The

decrease in the amount of nonprecipitating condensates also occurs when conditioned on high-precipitation percentiles (not shown). The amount of precipitating condensates on the other hand increases similarly in both sets of simulations (control to warm and control to fixed radiation) when conditioned on high precipitation percentiles, consistent with the increase in extreme precipitation rates. The lower concentrations of nonprecipitating condensates at upper levels lead to less export of cloud condensates by the circulation associated with precipitation extremes, and this may explain the greater increase in ϵ when the radiative cooling is held fixed.

In addition to affecting precipitation extremes, such a change in the amount of cloud condensates at high altitudes can potentially have a large impact on radiation and cloud–radiative feedback. Del Genio (2003) found that a nearly-neutral cloud feedback with warming in a set of climate model simulations resulted from a combination of opposing factors such as changes in precipitation efficiency and cloud-top heights. The fixed-radiation simulation is not very realistic in this regard because the radiative cooling profile is completely decoupled from the atmospheric temperatures. Nonetheless, the sensitivity of precipitation extremes and upper-tropospheric condensate amounts to the exact radiative cooling profile is notable (at least in this CRM with relatively simple microphysical parameterizations).

6. Changes in vertical velocities

We have shown that precipitation extremes are proportional to the associated vertical velocities, and that the vertical velocities do change in a warmer atmosphere. Vertical velocities are also closely related to the amount of lightning over land, which is one of the main causes of damage associated with extreme events (Del Genio et al. 2007). Furthermore the vertical velocity in a convecting plume affects the rate of detrainment of water condensates, therefore affecting the radiative effect of clouds, which is one of the least well-constrained climate feedbacks (Bony et al. 2006). It is therefore appropriate to analyze in more detail the changes in vertical velocities in our simulations, and to try to relate them to the changes in temperature and water mixing ratios.

The vertical velocities associated with precipitation extremes in the control and warm simulations are shown in Fig. 5. The shape of the profiles of instantaneous, hourly mean, and daily mean vertical velocities at those precipitation percentiles are strikingly similar, with simply weaker values as more time averaging is applied. The strength of the vertical velocities can decrease or increase depending on the vertical level considered, but the maximum vertical velocity over the column increases with

TABLE 2. Fractional changes in maximum (over the column) vertical velocities and $\sqrt{B}$ [given by (9)] at the 99.9th percentile of daily precipitation, and the fractional changes in reversible and pseudoadiabatic $\sqrt{CAPE}$ calculated based on horizontal and time mean temperature and moisture profiles. Changes are computed between the control simulation (SST = 300 K) and the warm simulation (SST = 305 K), and between the control simulation and the fixed-radiation warm simulation. Fractional changes are normalized by the SST change (i.e., all values are given in % K^{-1}).

	Control to warm (% K^{-1})	Control to fixed-radiation (% K^{-1})
w_{max} at 99.9th precipitation percentile	4.6	−5.6
Reversible $\sqrt{CAPE}$	3.8	0.8
Pseudoadiabatic $\sqrt{CAPE}$	4.1	2.3
$\sqrt{B}$ at 99.9th precipitation percentile	3.1	−11.0

warming (Table 2). This is not generally the case for the changes in vertical velocity from the control to the fixed-radiation simulation. For example, Fig. 7 shows that for precipitation extremes at daily time scales the maximum vertical velocity over the column decreases in magnitude with warming.

We note in passing that the maximum w over the column and the maximum of the pressure velocity $\omega \approx -\bar{\rho} g w$ over the column do not necessarily change in the same way. For instance, the hourly ω decreases with warming at all levels between the control and the warm simulation at the 99th precipitation percentile, despite an increase in maximum w. More generally, the maximum ω does not increase as much as the maximum w. This is important when comparing with changes in vertical velocities in climate models, since pressure velocities are typically reported for climate models.

Parodi and Emanuel (2009) have recently derived an expression for the vertical velocity in convective updrafts in terms of the terminal velocity of raindrops, the typical fluctuations in boundary layer entropy, and the difference in specific humidity inside and outside of clouds. We have been unable to confirm the applicability of this theory to our limited set of simulations because of the sensitivity of the results to the vertical level used for variables computed at one vertical level (e.g., w or the hydrometeor terminal velocity), and sensitivity to the vertical bounds for variables integrated vertically (e.g., buoyancy or condensate amount). Nonetheless, the theory does suggest an important role for condensate loading and terminal velocities in determining the maximum vertical velocity in updrafts, and these factors are likely to be relevant to the vertical velocities in our simulations of warming atmospheres.

In the absence of a closed theory for the vertical velocity that we can apply to the simulations, we instead make the first step of relating the changes in magnitude of the vertical velocities associated with precipitation extremes to changes in temperature and moisture variables. We will use two measures: the first and simplest measure that could be used in this context is the convective available potential energy (CAPE) based on horizontal and time mean temperature and moisture profiles. We calculate CAPE for parcels raised reversibly or pseudoadiabatically from the surface to their level of zero buoyancy z_{LZB}:

$$\text{CAPE} = \int_0^{z_{LZB}} g \frac{\alpha_p - \alpha_e}{\alpha_e} \, dz = \int_0^{z_{LZB}} g \left[\frac{T_p - T_e}{T_e} + \left(\frac{R_v}{R_d} - 1 \right) (q_{v,p} - q_{v,e}) - (q_{c,p} - q_{c,e}) - (q_{i,p} - q_{i,e}) \right] dz, \quad (8)$$

where α is the specific volume, q_v is the vapor mixing ratio, q_c is the cloud liquid mixing ratio, q_i is the cloud ice mixing ratio, R_d is the gas constant for dry air, and R_v is the gas constant for water vapor. Subscripts p and e refer to parcel and environmental properties, respectively. Our calculation of CAPE is consistent with the buoyancy and moist-thermodynamic formulations of the CRM.[3]

The second measure is the change in the vertically integrated buoyancy when the precipitation extremes occur [roughly following the first steps in the theory of Parodi and Emanuel (2009)]. From the vertical momentum equation (Khairoutdinov and Randall 2003), and assuming that all buoyancy yields vertical motion, we make the estimate $w_{max}^2/2 = B$, where

$$B = \int_{w=0}^{w=w_{max}} g \frac{\alpha'}{\alpha} \, dz$$
$$= \int_{w=0}^{w=w_{max}} g \left[\frac{T'}{\overline{T}} + \left(\frac{R_v}{R_d} - 1 \right) q_v' - q_n' - q_p' \right] dz, \quad (9)$$

where w_{max} is the maximum vertical velocity over the column, overbars denote spatial averages, primes denote departures from these averages, and all quantities are evaluated based on composite values associated with a particular percentile of precipitation. In other words, primes are departures from domain averages when the extremes occur. The mixing ratio of nonprecipitating condensates (cloud liquid and cloud ice) is denoted by q_n, and the mixing ratio of precipitating condensates (rain, graupel, and snow) is denoted by q_p. We integrate

vertically from the level where $w = 0$ in order to exclude the negatively buoyant air in cold pools near the surface.

The maximum of the vertical velocity over the column increases at a rate of 4.6% K^{-1} from the control to the warm simulation for velocities associated with the 99.9th percentile of daily precipitation (Table 2). This is similar to the rate of increase of both reversible and pseudoadiabatic $\sqrt{\text{CAPE}}$ (3.8% and 4.1% K^{-1}, respectively). (The CAPE is almost exactly the same in the simulations with double the spatial resolution.) However, CAPE fails at predicting the decrease in w_{max} between the control and fixed-radiation simulations, with w_{max} for the 99.9th percentile of daily precipitation decreasing by 5.6% K^{-1}, but reversible and pseudoadiabatic $\sqrt{\text{CAPE}}$ increasing by 0.8% and 2.3% K^{-1}, respectively.

As might be expected, the values of $\sqrt{2B}$ ($\sim$8 m s^{-1} at hourly time scales) are somewhat sensitive to the vertical bounds of the integration but are generally closer in magnitude to w_{max} ($\sim$3 m s^{-1} at hourly time scales) than $\sqrt{2\text{CAPE}}$ ($\sim$90 and $\sim$110 m s^{-1} for reversible and pseudoadiabatic CAPE, respectively). The fractional rates of change of w_{max} and $\sqrt{B}$ for the 99.9th percentile of daily precipitation are similar from the control to warm simulation (4.6% and 3.1% K^{-1}, respectively); they are not as similar from the control to fixed-radiation simulation (-5.6% and -11.0% K^{-1}, respectively), although the buoyancy based quantity B does at least predict that there is a decrease in vertical velocity in this case (Table 2).

For both CAPE and B, the contributions to buoyancy due to the temperature and water vapor anomalies [first and second terms on the right-hand sides of (8) and (9)] increase from the control to the warm simulation, while the condensate loading yields a decrease in buoyancy with warming due to increased condensate amounts. From the control to the fixed-radiation run, the decrease in B is due to a decrease in cloud temperature anomalies.

Thus, our results suggest that increased condensate loading does help limit updraft velocities under warming when the radiative profile is allowed to change consistent with the SST increase. But without a complete

---

[3] The lifted parcel conserves dry static energy $c_p T + gz$ below the lifted condensation level (LCL) and liquid/ice moist static energy $c_p T + gz - L_c q_c - L_s q_i$ and total water $q_c + q_i + q_v$ above the LCL, with the partition of condensates between q_i and q_c determined as a function of temperature as in the CRM. The reversible and pseudoadiabatic CAPE calculations differ by the condensate loading terms [last two terms in (8)], which are only included in the reversible CAPE computation. The effect of water on specific heat capacity is not included in the CRM.

theory for the dynamical changes with warming, we cannot properly attribute causes to the changes in vertical velocities.

7. Conclusions

We have used a cloud-resolving model to investigate the changes in precipitation extremes with warming in radiative–convective equilibrium. We find that the fractional increases in precipitation extremes are comparable in magnitude to the fractional increases in surface water vapor concentrations (i.e., they roughly follow Clausius–Clapeyron scaling based on the surface temperature). This seems to be at odds with the conclusions of the observational study of Allan and Soden (2008), who found that interannual variations of tropical precipitation extremes are more sensitive to temperature changes than Clausius–Clapeyron scaling would suggest. However, it could be that the vertical velocities associated with precipitation extremes respond differently to a horizontally uniform warming (as in this study) than to the large-scale changes in temperature and circulation associated with El Niño–Southern Oscillation. Our results are within the range of changes in tropical precipitation extremes found in different climate model simulations of global warming, since, depending on the climate model used, these can be much smaller or larger than what Clausius–Clapeyron scaling based on surface temperature would suggest (O'Gorman and Schneider 2009a).

To analyze the contributions to the changes in precipitation extremes with resolved convection, we have derived a simple expression for the precipitation rate that allows for convective-scale dynamics and condensate transports. This expression is derived from a dry static energy budget, and involves a precipitation efficiency that includes a contribution from the ratio of precipitation to net condensation. To first order, changes in precipitation extremes are well captured by a simplified scaling involving changes in the thermodynamics; changes in the dynamics play a secondary role, and tend to weaken the strength of precipitation extremes. Vertical velocities associated with precipitation extremes generally increase and shift upward, but they decrease where $\partial q_{sat}/\partial z$ is large in magnitude, yielding a negative contribution to the change in extreme precipitation rates.

What sets the strength of vertical velocities in convective updrafts remains an open question. We compared changes in updraft velocities to changes in CAPE (based on horizontal and time mean temperature and moisture profiles), and to an integrated measure of buoyancy when precipitation extremes occur B. Both CAPE and B increase from the control to the warm

simulation, despite a negative contribution from changes in condensate loading. These increases in CAPE and B are consistent with the greater overall magnitude of updraft velocities in the warm simulation, but as noted above, the upward shift of the vertical velocity profile must also be taken into consideration to account for changes in precipitation extremes.

The precipitation efficiency associated with precipitation extremes was largely unchanged from the control to the warm simulation. However, greater changes in precipitation efficiency were found in the "fixed radiation" comparison, and in simulations at different spatial resolutions. We also found that the imposed shear can affect changes in precipitation efficiency (not shown), so that it may not always be a good approximation to assume the precipitation efficiency is constant under warming. The sensitivity of our results to changes in the radiative cooling profile implies that we cannot rule out a dependence of changes in precipitation extremes on the exact details of the radiative and surface forcing. The greater changes in precipitation efficiency from the control to the fixed-radiation simulation seem to be related to large changes in the amount of condensates in the upper troposphere. The changes in condensate amount were evident in the time and horizontal mean condensates and would likely have important radiative impacts (at least in so far as they occur in this CRM). Although the fixed-radiation simulation is unrealistic by not allowing the radiation to respond to changing temperatures, it provides a useful counterpoint example of changing condensates and precipitation efficiency. The sensitivity of condensate concentrations to radiative and surface forcing in such simulations is worthy of further investigation.

It is reasonable to question whether our results would be very different if, for example, the spatial resolution was much higher so that updraft width was not constrained by the grid spacing, or if the convection occurred in an environment with either stronger or weaker shear. A contemporary study (Romps 2011) provides the opportunity to test the robustness of our conclusions to various modeling choices and methods of analysis. Both studies investigate the effect of warming on precipitation extremes in simulations of radiative-convective equilibrium with resolved convection, but with several important differences in model configuration. The domain used in (Romps 2011) is much smaller (25.6 vs 1024 km), but with much higher resolution (200 m vs 4 km), and the warming results from increased CO_2 concentrations rather than specified changes in SST. Despite these and other differences, we reach the common conclusion that the amplification of precipitation extremes with warming scales approximately with surface water vapor concentrations, and that the precipitation

efficiency remains approximately constant. In both analyses, the relevant dynamical quantity for precipitation extremes is not the vertical velocity at a given level or its maximum, but an integral measure of w. The results regarding the dynamical contributions to precipitation differ; in the (Romps 2011) decomposition, the dynamical contribution to precipitation extremes, as measured by condensation-weighted vertical integrals, increases with warming whereas in our case the dynamical contribution to precipitation extremes, as measured by $\partial q_{sat}/\partial z$-weighted vertical integrals, decreases. Nevertheless, both studies find that convection extends to higher altitudes with warming, as expected from the upward shift of the radiative cooling profile (Figs. 8a,d), and that the strongest updraft velocities become even stronger with warming.

We have investigated the response of precipitation extremes to warming in an idealized setting. As discussed in the introduction, other factors affect precipitation extremes, including large-scale dynamics, land–ocean contrasts, orography, the diurnal cycle, mesoscale organization, and radiation–convection interactions. Since these factors would impact precipitation extremes both in the control and in the warm climate, their net effect on the amplification of precipitation extremes is not straightforward, and deserves further investigation, perhaps using CRM simulations to isolate the effects of the processes involved. Our work could provide a useful framework for distinguishing between thermodynamic, dynamic, and microphysical contributions to how these factors influence precipitation extremes in a warming climate.

REFERENCES

Allan, R. P., and B. J. Soden, 2008: Atmospheric warming and the amplification of precipitation extremes. *Science,* **321** (5895), 1481–1484.

Allen, M. R., and W. J. Ingram, 2002: Constraints on future changes in climate and the hydrologic cycle. *Nature,* **419,** 224–232.

Betts, A. K., 1998: Climate-convection feedbacks: Some further issues. *Climatic Change,* **39,** 35–38.

Bony, S., and Coauthors, 2006: How well do we understand and evaluate climate change feedback processes? *J. Climate,* **19,** 3445–3482.

Bretherton, C. S., M. E. Peters, and L. E. Back, 2004: Relationships between water vapor path and precipitation over the tropical oceans. *J. Climate,* **17,** 1517–1528.

Del Genio, A. D., 2003: The global water cycle and climate change. *Extended Abstracts, Third GPM Workshop: Consolidating the Concept,* Noordwijk, Netherlands, ESTEC. [Available online at http://esamultimedia.esa.int/conferences/03C06/abstracts/s311.pdf.]

——, M.-S. Yao, and J. Jonas, 2007: Will moist convection be stronger in a warmer climate? *Geophys. Res. Lett.,* **34,** L16703, doi:10.1029/2007GL030525.

Emori, S., and S. J. Brown, 2005: Dynamic and thermodynamic changes in mean and extreme precipitation under changed climate. *Geophys. Res. Lett.,* **32,** L17706, doi:10.1029/2005GL023272.

Fu, Q., S. K. Krueger, and K. N. Liou, 1995: Interactions of radiation and convection in simulated tropical cloud clusters. *J. Atmos. Sci.,* **52,** 1310–1328.

Hartmann, D. L., and K. Larson, 2002: An important constraint on tropical cloud–climate feedback. *Geophys. Res. Lett.,* **29,** 1951, doi:10.1029/2002GL015835.

Held, I. M., and B. J. Soden, 2006: Robust responses of the hydrological cycle to global warming. *J. Climate,* **19,** 5686–5699.

Iribarne, J. V., and W. L. Godson, 1981: *Atmospheric Thermodynamics.* 2nd ed. D. Reidel, 25 pp.

Khairoutdinov, M. F., and D. A. Randall, 2003: Cloud-resolving modeling of the arm summer 1997 IOP: Model formulation, results, uncertainties, and sensitivities. *J. Atmos. Sci.,* **60,** 607–625.

Kharin, V. V., F. W. Zwiers, X. Zhang, and G. C. Hegerl, 2007: Changes in temperature and precipitation extremes in the IPCC ensemble of global coupled model simulations. *J. Climate,* **20,** 1419–1444.

Kuang, Z., and D. L. Hartmann, 2007: Testing the fixed anvil temperature hypothesis in a cloud-resolving model. *J. Climate,* **20,** 2051–2057.

Leary, C. A., and R. A. Houze, 1979: The structure and evolution of convection in a tropical cloud cluster. *J. Atmos. Sci.,* **36,** 437–457.

Lenderink, G., and E. van Meijgaard, 2008: Increase in hourly precipitation extremes beyond expectations from temperature changes. *Nat. Geosci.,* **1,** 511–514.

Liu, S. C., C. Fu, C.-J. Shiu, J.-P. Chen, and F. Wu, 2009: Temperature dependence of global precipitation extremes. *Geophys. Res. Lett.,* **36,** L17702, doi:10.1029/2009GL040218.

Muller, C. J., L. E. Back, P. A. O'Gorman, and K. A. Emanuel, 2009: A model for the relationship between tropical precipitation and column water vapor. *Geophys. Res. Lett.,* **36,** L16804, doi:10.1029/2009GL039667.

Neelin, J., O. Peters, and K. Hales, 2009: The transition to strong convection. *J. Atmos. Sci.,* **66,** 2367–2384.

O'Gorman, P. A., and T. Schneider, 2008: The hydrological cycle over a wide range of climates simulated with an idealized GCM. *J. Climate,* **21,** 3815–3832.

——, and ——, 2009a: The physical basis for increases in precipitation extremes in simulations of 21st-century climate change. *Proc. Natl. Acad. Sci. USA,* **106,** 14 773–14 777.

——, and ——, 2009b: Scaling of precipitation extremes over a wide range of climates simulated with an idealized GCM. *J. Climate,* **22,** 5676–5685.

——, and C. J. Muller, 2010: How closely do changes in surface and column water vapor follow Clausius-Clapeyron scaling in climate change simulations? *Environ. Res. Lett.,* **5,** 025207, doi:10.1088/1748-9326/5/2/025207.

Pall, P., M. R. Allen, and D. A. Stone, 2007: Testing the Clausius-Clapeyron constraint on changes in extreme precipitation under CO_2 warming. *Climate Dyn.,* **28,** 351–363.

Parodi, A., and K. A. Emanuel, 2009: A theory for buoyancy and velocity scales in deep moist convection. *J. Atmos. Sci.,* **66,** 3449–3463.

Pauluis, O., and S. Garner, 2006: Sensitivity of radiative-convective equilibrium simulations to horizontal resolution. *J. Atmos. Sci.,* **63,** 1910–1923.

Roe, G. H., 2005: Orographic precipitation. *Annu. Rev. Earth Planet. Sci.,* **33,** 645–671.

Romps, D. M., 2011: Response of tropical precipitation to global warming. *J. Atmos. Sci.,* **68,** 123–138.

Stephens, G. L., and T. D. Ellis, 2008: Controls of global-mean precipitation increases in global warming GCM experiments. *J. Climate,* **21,** 6141–6155.

Sugiyama, M., H. Shiogama, and S. Emori, 2010: Precipitation extreme changes exceeding moisture content increases in MIROC and IPCC climate models. *Proc. Natl. Acad. Sci. USA,* **107,** 571–575.

Trenberth, K. E., 1999: Conceptual framework for changes of extremes of the hydrological cycle with climate change. *Climatic Change,* **42,** 327–339.

Vecchi, G. A., and B. J. Soden, 2007: Global warming and the weakening of the tropical circulation. *J. Climate,* **20,** 4316–4340.

Wilcox, E. M., and L. J. Donner, 2007: The frequency of extreme rain events in satellite rain-rate estimates and an atmospheric general circulation model. *J. Climate,* **20,** 53–69.

Williams, E., T. Chan, and D. Boccippio, 2004: Islands as miniature continents: Another look at the land-ocean lightning contrast. *J. Geophys. Res.,* **109,** D16206, doi:10.1029/2003JD003833.